Extension of the full-folding optical model for nucleon-nucleus scattering with applications up to 1.5 GeV

H. F. Arellano
Departamento de Física, Facultad de Ciencias Físicas y Matemáticas, Universidad de Chile, Casilla 487-3, Santiago, Chile

H. V. von Geramb
Theoretische Kernphysik, Universität Hamburg, Luruper Chaussee 149, D-22761, Hamburg, Germany
(Received 10 April 2002; published 2 August 2002)

The nonrelativistic full-folding optical model approach for nucleon-nucleus scattering is extended into the relativistic regime. In doing so, kinematical issues involving the off-shell Lorentz boost of the colliding particles between the two nucleons and the projectile-nucleus center-of-mass reference frames have been taken into account. The two-body effective interaction is obtained in the framework of the nuclear matter *g* matrix using nucleon-nucleon optical model potentials that fully account for the inelasticities and isobar resonances in the continuum at nucleon energies up to 3 GeV. Diverse nucleon-nucleon (*NN*) potential models were constructed by supplementing the basic Paris, Nijmegen, Argonne, or Gel'fand-Levitan-Marchenko inversion potentials with complex separable terms. In each case the additional separable terms ensured that the combination led to *NN* scattering phase shifts in excellent agreement with experimental values. With each phase shift fitting potential nuclear matter *g* matrices have been formed and with each of those relativistic full-folding optical potentials for nucleon-nucleus elastic scattering determined. Application to such scattering for projectile energies up to 1.5 GeV have been made. Good and systematic agreement is obtained between the calculated and measured observables, both differential and integrated quantities, over the whole energy range of our study. A moderate sensitivity to off-shell effects in the differential scattering observables also is observed.

DOI: 10.1103/PhysRevC.66.024602 PACS number(s): 03.65.Nk, 25.40.Cm, 24.10.−i

I. INTRODUCTION

Elastic nucleon-nucleus (*NA*) scattering is known now as an excellent means of testing nuclear structure [1]. Results of the nonrelativistic theory for such scattering confidently can be used as predictive for information required in applied nuclear technology, where large amounts of nuclear reaction data—including fission cross sections at intermediate energies—are required for various challenging applications such as accelerator transmutation of waste, particularly the elimination of long-lived radioactive wastes with a spallation source, accelerator-based conversion to destroy weapon grade plutonium, accelerator-driven energy production to derive fission energy from thorium with concurrent destruction of the long-lived waste and without the production of nuclear weapon material, and accelerator production of tritium [2]. There is also a great need for such information to be the base in analyzes of patient radiation therapy and protection.

With basic science there is the intellectual challenge to go beyond the physics of a single hadron and understand essential aspects of nuclear physics from first principles such as QCD [3]. It is generally agreed that the QCD Lagrangian involves nonlinear dynamics. This makes it very difficult then to understand nuclear physics fully from first principles, and so most of nuclear physics phenomena are interpreted in terms of appropriate effective degrees of freedom. One such view of natural phenomena in terms of energy scales (Q) divides the nuclear-hadronic scale into the nuclear structure region $Q \sim 1-10$ MeV and the nucleon and nucleon-nucleon (*NN*) region, with structure and substructure scales $Q \sim 0.3-1$ GeV. This large separation between the hadronic energy scale and the nuclear binding scale poses stringent difficulties to apply nonlinear QCD directly to understand the physics of nuclei. However, quantitative calculations based on effective quantum field theory (EQF) techniques that arise from chiral symmetry provide an alternative approach. At present, this method is being extended to address few- and many-nucleon interactions. When combined with first principle calculations of the low energy constants from QCD, these EQF may provide a consistent qualitative understanding of properties of nuclei and of low to medium energy nuclear scattering.

Besides understanding the structure of nuclei from a QCD point of view, it is of interest to understand the dynamical behavior of nucleons in the presence of nuclear matter. The relevance of modified *NN* scattering amplitudes in the form of *g* matrices in the nuclear medium with mean fields and Pauli blocking is well known. These *NN* amplitudes and alternative reductions—in the form of *t* matrices—have been used with qualitative success in the specification of nuclear densities in stable nuclei and the description of *NA* scattering for projectile energies ($T_{\rm lab}$) below 1 GeV. For $T_{\rm lab}$ above this limit we expect significant dynamical changes due to dibaryonic fusion with subsequent fission in the short range region of *NN* subsystems [4].

Hitherto quite independently, several groups successfully described intermediate energy *NA* scattering using two nucleon *t* or *g* matrices as driving effective interactions [5]. Among them we distinguish two main philosophies under which a description of *NA* collisions is made and which we specify as the nonrelativistic Schrödinger approach and as the relativistic Dirac approach [1,5]. Common to both is the explicit use, and accurate treatment, of an interacting *NN* pair in the realm of other nucleons in a nucleus, and the need for

an effective *NN* scattering amplitude known and defined on- and off-shell. For the more recent calculations of nonrelativistic *NA* optical potentials in momentum space [6–8], a consistent treatment of the fully off-shell *NN* t or g matrices have been used.

As nearly all available *NN* potentials [9–12] have been fitted to *NN* scattering data up to 350 MeV, a nonrelativistic treatment of the full-folding optical model suffices for most *NA* scattering applications consistent with the input *NN* model. Recently, however, inversion potentials developed to fit elastic *NN* phase shifts for $T_{\rm lab}<1.2$ GeV have been used within the full-folding approach for projectile energies as high as 500 MeV [13]. Despite the fact that these were nonrelativistic applications, they allowed a better description of data relative to what was found previously using traditional *NN* potential models. The lack of relativistic kinematics as well as pion production and Δ excitations within the *NN* pair did not manifest itself as a dramatic limitation of the model, even though the theoretical confidence level was reached. It is the primary aim of this work to remove these shortcomings and formulate a momentum space full-folding model using *minimum relativity*. With the appropriate modifications to the existing analysis programs we expect to extend the confidence level into the GeV region and to obtain high quality full-folding optical model results at energies as high as 1.5 GeV.

Extensive studies of *NA* scattering in the context of relativistic Dirac models have been made [5,14–17]. While these models are closer to a fundamental formulation with the inclusion of relativistic kinematics and dynamics within a single framework, to date they all have used fitted *NN* interactions that do not describe the phase shift data well. This is a serious drawback as it is well established that any folding model requires a high quality *NN* interaction as input.

The description of *NA* scattering requires only modest nuclear matter densities, and thus the need of *NN* g matrices is less demanding. Furthermore only for projectile energies below 500 MeV are nuclear medium effects predominant with specific treatment of Pauli blocking and self consistent mean field effects being crucial. For medium and higher *NN* energies, meson production and intrinsic hadron excitations within the interacting pair are important. Consequently the t matrix no longer is unitary in the elastic channel. However, as the low energy t and g matrices are well defined within potential scattering theory, we seek a continuation of *NN* potential models with an *NN* optical model potential (NNOMP). We have devised and generated NNOMP for $0.3<T_{\rm lab}<3$ GeV and applied them to *NA* elastic scattering. The calculations are based upon a relativistically corrected full-folding optical model in momentum space that is an extension of a nonrelativistic predecessor [6]. Since the Lorentz contraction scales as the ratio of the projectile energy to its mass, it requires nucleon projectile energies above 400 MeV to have sizable contraction effects. It is safe to include relativistic kinematics in folding calculations when the projectile energy surpasses 300 MeV. Relativistic kinematics is widely used in pion-nucleus scattering [18–22]. An excellent discussion on some aspects about relativistic kinematics in *NA* scattering is given in the review by Ray, Hoffmann, and Coker [5].

One of the important advantages of finding a nonrelativistic *NA* optical model potential is its well-defined structure in terms of interacting nucleon pairs. This framework has been remarkably successful in the study of low energy scattering with its link to the nuclear shell model of single particle bound states. The combination of target correlations and high quality *NN* interactions has provided a good first order description of the *NA* dynamics. This nonrelativistic theoretical approach has been applied with success for many energies and targets, and now it is timely to incorporate relativistic corrections so that calculations can be made with energies as high as 1.5 GeV.

A brief summary of the current full-folding optical model is given in Sec. II and in which the points where relativistic kinematic corrections are to be made are stressed. The current experimental situation of *NN* phase shift analysis up to 3 GeV is discussed in Sec. III. We describe also how the NNOMP are determined by the *NN* phase shift data. In Sec. IV we set the framework of the g-matrix calculations and specify minimal relativity considerations. In Sec. V some details of the full-folding calculations and various applications are presented. We discuss the role of the Fermi motion in the *NN* effective interaction and analyze the sensitivity of *NA* scattering observables upon the use of alternative approaches for the relativistic kinematics. We also examine total cross sections for nucleon elastic scattering and differential observables at beam energies from the hundreds of MeV up into the GeV regime. Section VI contains a summary and the main conclusions of our study. Finally, we have included two Appendixes. In Appendix A the relativistic kinematics transformations in the context of the full-folding approach are outlined as extracted from the articles by Aaron, Amado, and Young [20] and by Giebink [22]. In Appendix B we present the algorithm we have used to determine the NNOMP from data.

II. FULL-FOLDING FRAMEWORK

In the nonrelativistic theory of the optical model potential, the coupling between the projectile and the target nucleus in the elastic channel is given by the convolution between a two-body effective interaction and the target ground-state mixed density. In the projectile-nucleus center-of-mass (c.m.) frame, the collision of a projectile of kinetic energy E is described by the optical potential $U(E)$ which in a momentum space representation is expressed as [6]

$$U(\mathbf{k}',\mathbf{k};E)=\sum_{\alpha\leqslant\epsilon_F}\int\int d\mathbf{p}'\,d\mathbf{p}\,\phi_\alpha^\dagger(\mathbf{p}') \times\langle\mathbf{k}'\mathbf{p}'|\mathcal{T}(\Omega_\alpha)|\mathbf{k}\mathbf{p}\rangle_{A+1}\phi_\alpha(\mathbf{p}), \quad (1)$$

where ϕ_α represents target ground state single-particle wave functions of energy ϵ_α, and $\alpha\leqslant\epsilon_F$ restricts the sum to all levels up to the Fermi surface ϵ_F. The two-body $\mathcal{T}$ matrix is evaluated at starting energies $\Omega_\alpha=m_p+E+m_t+\epsilon_\alpha$ consisting of the mass of the projectile m_p, its kinetic energy E, the

mass of the target nucleon m_t and its binding energy ϵ_α. The subscript $A+1$ indicates matrix elements in the projectile-nucleus c.m. frame and recoil effects have been neglected for simplicity. In the most recent full-folding calculations of the optical potential for *NA* scattering, where explicit medium effects are incorporated in the two-body effective interaction, the $\mathcal{T}$ matrix is represented by an infinite nuclear matter g matrix [6]. In the absence of these medium modifications, the $\mathcal{T}$ matrix has usually been approximated by the two-body scattering matrix associated with the collisions of two free particles [6,7]. None of these full-folding approaches incorporate the necessary relativistic kinematics needed for high energy processes.

The above expression for the optical potential requires the $\mathcal{T}$ matrix in the projectile-nucleus c.m. frame. However, most practical two-body potential models are designed to account for the scattering data in the two-body c.m., where a one-body wave equation (a Schrödinger kind equation) is used to construct the realistic two-body bare potential fit to elastic scattering and ground state data. The practical problem that emerges then is how to make use of this description to extract the needed effective interaction in the projectile-nucleus c.m. with an adequate account of relativistic effects. This has been a long standing problem in nuclear research and various approaches have been proposed and discussed elsewhere [18–22]. In the procedure followed here we retain the dynamical structure of the optical potential as expressed by Eq. (1) and identify, *via* a Lorentz boost, the corresponding kinematical variables involved in the two-body collision. Thus, the transformation of the $\mathcal{T}$ matrix from the two-body (2B) to the projectile-nucleus $(A+1)$ c.m. frame can be done by considering three separate aspects. First, as Lorentz invariance of the flux is required, an overall normalization factor—usually referred as the Møller flux factor—mediates between the scattering amplitudes in the two frames. Second, the kinematics in the projectile-nucleus c.m. frame needs to be transformed to the two-body c.m. system, which is the reference frame where the bare potential model is defined. And third, the transformation of the scattering matrix from the two-body to the projectile-nucleus c.m. frames involves the rotation of the spins, an effect referred as the Wigner rotation. This contribution has been studied in the context of the relativistic ''no-pair'' potential for nucleon-nucleus scattering by Tjon and Wallace [16] and was observed to yield rather moderate effects at nucleon energies between 200 and 500 MeV. Although there is no statement about the importance of Wigner rotation contribution at the higher energies considered here, we shall neglect them in the present work.

Consistent with the notation introduced in Fig. 1 for the coupling between the projectile and the target-struck nucleon, we denote their respective incoming and outgoing four-momenta:

$$k=(\bar{\omega},\mathbf{k}),\quad k'=(\bar{\omega}',\mathbf{k}');\quad p=(\bar{\varepsilon},\mathbf{p}),\quad p'=(\bar{\varepsilon}',\mathbf{p}'). \tag{2}$$

When translational invariance is assumed, as in the case of free or particles in infinite nuclear matter, the two-body interaction is characterized by the starting energy Ω and the total momentum of the colliding particles $\mathbf{Q}$,

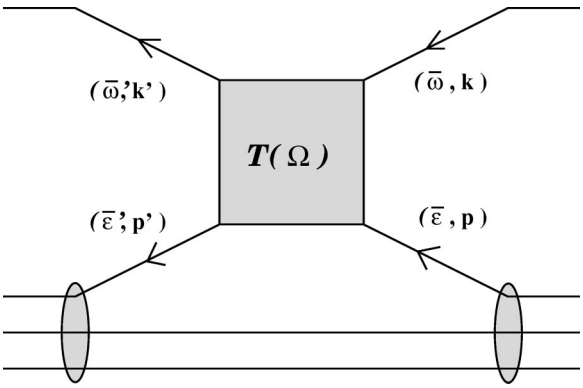

FIG. 1. Schematic representation of the collision of the projectile with a target nucleon. Quantities in parentheses represent the four-momenta of the colliding nucleons.

$$\begin{aligned}\langle \mathbf{k}'\mathbf{p}'|\mathcal{T}(\Omega)|\mathbf{k}\mathbf{p}\rangle_{A+1} &= \eta(\mathbf{k}'\mathbf{p}';\mathbf{k}\mathbf{p})\\ &\times\langle \mathbf{k}_r',-\mathbf{k}_r'|\tau_{\mathbf{Q}}(\sqrt{s})|\mathbf{k}_r,-\mathbf{k}_r\rangle_{2B}\\ &\times\delta(\mathbf{Q}'-\mathbf{Q}).\end{aligned} \tag{3}$$

Here the Dirac δ function makes explicit the total three-momentum conservation of the two-body collision, $\mathbf{Q}'=\mathbf{Q}$, where

$$\mathbf{Q}=\mathbf{k}+\mathbf{p},\quad \mathbf{Q}'=\mathbf{k}'+\mathbf{p}', \tag{4}$$

and $\sqrt{s}$ represents the energy in two-body c.m.,

$$s=\Omega^2-\mathbf{Q}^2. \tag{5}$$

The overall coefficient η is the Møller flux factor,

$$\eta(\mathbf{k}'\mathbf{p}';\mathbf{k}\mathbf{p})=\left[\frac{\omega(\mathbf{k}_r')\varepsilon(-\mathbf{k}_r')\omega(\mathbf{k}_r)\varepsilon(-\mathbf{k}_r)}{\omega(\mathbf{k}')\varepsilon(\mathbf{p}')\omega(\mathbf{k})\varepsilon(\mathbf{p})}\right]^{1/2}, \tag{6}$$

where the energies ω and ε are on-mass-shell, i.e., $\omega^2=m_p^2+\mathbf{k}_r^2$ and $\varepsilon^2=m_t^2+\mathbf{k}_r^2$.

What remains to be specified is a Lorentz transformation for the relative momenta $\mathbf{k}_r$ and $\mathbf{k}_r'$. To this purpose we followed the approaches introduced by Aaron, Amado, and Young (AAY) [20] and Giebink [22]. Although, both assume a representation of the scattering matrix in the two-body c.m., they differ in the way the Lorentz boost is devised. Details are given in Appendix A, where we show that in both cases the relative momenta can be cast into the form

$$\mathbf{k}_r=W\mathbf{k}-(1-W)\mathbf{p},\quad \mathbf{k}_r'=W'\mathbf{k}'-(1-W')\mathbf{p}', \tag{7}$$

with W and W' being functions of the momenta of the colliding particles [Eq. (A4) or (A11)]. At low beam energies both prescriptions meet the nonrelativistic limit $W\sim W'\sim m_p/(m_p+m_t)$, as expected.

III. THE *NN* OPTICAL MODEL POTENTIAL

Of the whole spectrum, low and medium energy *NN* scattering traditionally is described in terms of Hermitian potentials. At medium energies, production processes and inelasticities become possible and several elementary systems composed of nucleons and mesons contribute to *NN* scattering. At present there is no high quality description of *NN* scattering above the inelastic threshold either in terms of QCD or in terms of nucleons and mesons.

A high quality fit of on-shell *t* matrices by means of a potential model is very desirable as it provides extensions of the effective interaction into the off-shell domain and into a nuclear medium, which are important dynamical features in few and many body calculations. Many examples using microscopic optical model potentials for elastic nucleon-nucleus scattering and bremsstrahlung reactions have shown that it is crucial to have on-shell *t* matrices in the best possible agreement with *NN* data at all energies. Concomitantly one needs high precision *NN* data against which one can specify *NN* interactions. To this purpose we have relied on a large body of experimental *NN* data whose parametrization in terms of amplitudes and phase shifts are smooth for energies to 3 GeV [23]. This is a supposition for the construction of an *NN* potential above 300 MeV.

There are many studies of few and many body problems in the low energy regime $T_{\rm lab}<300$ MeV and the results have consequences for any model extension above threshold. We note in this context that significant off-shell differences in *t* matrices are known to exist among the theoretically well motivated boson exchange models of *NN* scattering. It remains difficult to attribute with certainty any particular dynamical or kinematical feature with those differences. Nonlocality, explicit energy dependence, and features associated with relativistic kinematics are some possibilities. In contrast, there is the quantum inverse scattering approach by which on-shell *t* matrices can be continued into the off-shell domain. A specific method is the Gel'fand-Levitan-Marchenko inversion algorithm for Sturm-Liouville equations. This approach to specify *t* matrices off-shell is appropriate when the physical *S* matrix is unitary and the equation of motion is of the Sturm-Liouville type. Such is valid without modification for *NN t* matrices in the energy regime below 300 MeV, and for the unitary part of the *S* matrix above that energy.

In the spirit of general inverse problems, we have extended the available low energy potential by additional complex potential terms which are determined from a perfect reproduction of the experimental data (here the partial wave phase shift analysis) for all energies above 300 MeV. This means that *NN* optical models were generated separately for each partial wave. The algorithm we have developed allows studies of complex local and/or separable potentials in combination with any background reference potential [4,24]. Here we limit the reference potential to the well known real coordinate space potentials from Paris [9], Nijmegen [10] (Reid93, Nijmegen-I, Nijmegen-II), Argonne [11] (AV18), and from inversion [25]. To them we add channel-dependent complex separable potentials with energy dependent strengths [4]. For a given input data set there is a unique NNOMP within a given potential class. Some of these issues are outlined in Appendix B.

NN scattering is a long standing problem which has been reviewed often as the database developed. The low energy data has been analyzed by the Virginia group [23] for $T_{\rm lab}\leqslant 400$ MeV, the Nijmegen group with the *NN* partial-wave phase shift analysis for $T_{\rm lab}\leqslant 350$ MeV [10], and by Machleidt [12] giving the Bonn-CD-2000. Of these, the Virginia group has given many solutions over the years, the latest are for energies up to 3 GeV [26]. We have used their SP00, FA00, and WI00 solutions in our calculations and found results that differ but only marginally. Thus hereafter in the main we refer solely to the results of calculations based upon the SP00 solution.

As with the *NN* phase shift analysis, one boson exchange potentials have received several critical reviews [12], including observations that there are small variations between phase shift analysis and potential models below the subthreshold domain $T_{\rm lab}<300$ MeV. A theoretically stable result would require many quantities that need be specified *a priori*, to be determined by independent sources. At present that does not seem feasible and all current potentials rely upon fits of many of their parameters to the same data. All such fits, however, have been made independently of each other and are based upon differing theoretical specifications of the boson exchange model dynamics.

Above 300 MeV, reaction channels open and the elastic channel *S* matrix no longer is unitary. Only the $\Delta(1232)$ resonance has a low energy threshold and a relative small width of 120 MeV. Therefore it is the only resonance we expect to be obviously visible in the energy variation of the elastic scattering phase shifts. In particular one notices typical variations in the ${}^1D_2$, ${}^3F_3$, and ${}^3PF_2$ channels. Otherwise the phase shifts to 3 GeV vary smoothly as functions of energy. Together with the strong spin-isospin coupling, this property infers optical potentials that are channel dependent in contrast to the *NA* case for which assumed central and spin-orbit potentials are partial wave independent. The plethora of reaction channels that open to 3 GeV, and the requirement of an *NN* optical potential prescription, mean that it is an interesting task for a microscopic model to link QCD substructures to *NN* scattering phase shift functions in analogy to that successful prescription by which *NA* optical potentials have been determined by folding effective interactions.

To describe this developing system for $0.3<T_{\rm lab}<3$ GeV we used Feshbach theory to specify the optical potential. An important feature of that theory is the projection operator formalism with *P* and *Q* subspaces, which divide the complete Hilbert space $(P+Q)$ into the elastic scattering channel, the *P* space, and the inelastic and reaction channels, the *Q* space. This infers a complex and separable component in the optical potential with an energy dependent strength. If a very large number of intermediate states contribute, the effect equates to a local potential operator.

A covariant description of *NN* scattering formally is given by the Bethe-Salpeter equation

$$\mathcal{M}=\mathcal{V}+\mathcal{V}G\mathcal{M}, \tag{8}$$

where $\mathcal{M}$ are invariant amplitudes that are based upon all connected two particle irreducible diagrams. This equation serves generally as an ansatz for approximations. Of those, the three-dimensional Blankenbecler-Sugar (BbS) reduction is popular and sufficient for our purpose to define an *NN* potential [12]. The amplitudes are now expressed with the reduced terms and they satisfy a three-dimensional equation

$$\mathcal{M}(\mathbf{q}',\mathbf{q}) = \mathcal{V}(\mathbf{q}',\mathbf{q}) + \int \frac{d^3k}{(2\pi)^3} \mathcal{V}(\mathbf{q}',\mathbf{k}) \times \frac{M^2}{E_{\mathbf{k}}} \frac{\Lambda^+_{(1)}(\mathbf{k})\Lambda^+_{(2)}(-\mathbf{k})}{\mathbf{q}^2-\mathbf{k}^2+i\varepsilon} \mathcal{M}(\mathbf{k},\mathbf{q}). \tag{9}$$

Taking matrix elements with only positive energy spinors, an equation with minimum relativity results for the *NN t* matrix, namely

$$\mathcal{T}(\mathbf{q}',\mathbf{q}) = \mathcal{V}(\mathbf{q}',\mathbf{q}) + \int \frac{d^3k}{(2\pi)^3} \mathcal{V}(\mathbf{q}',\mathbf{k}) \frac{M^2}{E_{\mathbf{k}}} \frac{1}{\mathbf{q}^2-\mathbf{k}^2+i\varepsilon} \mathcal{T}(\mathbf{k},\mathbf{q}). \tag{10}$$

Using the substitutions

$$T(\mathbf{q}',\mathbf{q}) = \left(\frac{M}{E_{\mathbf{q}'}}\right)^{1/2} \mathcal{T}(\mathbf{q}',\mathbf{q}) \left(\frac{M}{E_{\mathbf{q}}}\right)^{1/2} \tag{11}$$

and

$$V(\mathbf{q}',\mathbf{q}) = \left(\frac{M}{E_{\mathbf{q}'}}\right)^{1/2} \mathcal{V}(\mathbf{q}',\mathbf{q}) \left(\frac{M}{E_{\mathbf{q}}}\right)^{1/2}, \tag{12}$$

a simplified form of the *t* matrix is obtained. It is the familiar Lippmann-Schwinger equation

$$T(\mathbf{q}',\mathbf{q}) = V(\mathbf{q}',\mathbf{q}) + \int \frac{d^3k}{(2\pi)^3} V(\mathbf{q}',\mathbf{k}) \frac{M}{\mathbf{q}^2-\mathbf{k}^2+i\varepsilon} T(\mathbf{k},\mathbf{q}). \tag{13}$$

The strategic importance of this result is that it defines a sensible continuation of a *t* matrix, constrained on-shell by the experimental data and phase shift analysis, into the off-shell domain as required by the full-folding optical model. Thus we do not rely primarily on a fundamental theoretical result but rather on experimental *NN* data and the moderate sensitivity of *NA* scattering to alternative off-shell continuations. It is an important result also of this analysis that on-shell equivalent *NN* optical model potentials yield very similar *NA* scattering observables—irrespectively of differences in the off-shell domain and the constraint off-shell continuation defined with Eqs. (9)–(13).

IV. IN-MEDIUM EFFECTIVE INTERACTION

A crucial step in the description of *NA* scattering processes has been the definition of an effective interaction based on the bare two-body interaction in free space. Such has been the philosophy of the early (local) folding models and the most recent nonrelativistic full-folding models [6]. The effective interaction, $\mathcal{T}$ in Eq. (1), is obtained in the framework of Brueckner-Bethe-Goldstone for the *g* matrix. The extension of this approach to high energy applications requires a minimal account of relativistic corrections. Along this line we have followed the discussion by Brockmann and Machleidt [27], where a relativistic three-dimensional reduction of the Bethe-Salpeter equation is used to describe the interaction between nucleons in the nuclear medium. If only matrix elements between positive-energy spinors are taken, then the medium-modified invariant amplitude in an arbitrary frame reads [cf. Eqs. (A17) and (A18) in Ref. [27]]

$$\mathcal{G}_{\mathbf{Q}}(\mathbf{q}',\mathbf{q};s) = \mathcal{V}_{\mathbf{Q}}(\mathbf{q}',\mathbf{q}) + \int \frac{d^3k}{(2\pi)^3} \mathcal{V}_{\mathbf{Q}}(\mathbf{q}',\mathbf{k}) \left(\frac{M}{E_{(1/2)\,\mathbf{Q}+\mathbf{k}}}\right) \times \frac{M\overline{Q}(\mathbf{Q};\mathbf{k})}{\frac{1}{4}s + \frac{1}{4}\mathbf{Q}^2 - E^2_{(1/2)\,\mathbf{Q}+\mathbf{k}} + i\varepsilon} \mathcal{G}_{\mathbf{Q}}(\mathbf{k},\mathbf{q};s). \tag{14}$$

Here the momentum $\mathbf{Q}$ represents the momentum of the pair with respect to the background, and $\overline{Q}$ the Pauli blocking operator which projects onto unoccupied intermediate states. For the above expression angle averages have been used, i.e., $|\frac{1}{2}\mathbf{Q}+\mathbf{k}|^2 \approx \frac{1}{4}\mathbf{Q}^2+\mathbf{k}^2$, and the *s* invariant has been defined as $s = 4E^2_{(1/2)\mathbf{Q}+\mathbf{q}} - \mathbf{Q}^2$. This approach, in the context of the Dirac-Brueckner-Hartree-Fock approximation, has been applied with reasonable success to the study of infinite nuclear matter [27] as well as finite nuclei ground state properties [28].

An appealing feature of the above equation for $\mathcal{G}$ is its direct connection with the bare *NN* potential model in free space. Indeed, adopting the same definitions as in Eqs. (11) and (12),

$$g_{\mathbf{Q}}(\mathbf{q}',\mathbf{q};\sqrt{s}) = \sqrt{\frac{M}{E_{\mathbf{q}'}}} \mathcal{G}_{\mathbf{Q}}(\mathbf{q}',\mathbf{q};s) \sqrt{\frac{M}{E_{\mathbf{q}}}} \tag{15}$$

and

$$V(\mathbf{q}',\mathbf{q}) = \sqrt{\frac{M}{E_{\mathbf{q}'}}} \mathcal{V}(\mathbf{q}',\mathbf{q}) \sqrt{\frac{M}{E_{\mathbf{q}}}}, \tag{16}$$

the following equation for the *g* matrix is obtained:

$$g_{\mathbf{Q}}(\mathbf{q}',\mathbf{q};\sqrt{s}) = V_{\mathbf{Q}}(\mathbf{q}',\mathbf{q}) + \int \frac{d^3k}{(2\pi)^3} V_{\mathbf{Q}}(\mathbf{q}',\mathbf{k}) \left(\frac{E_{\mathbf{k}}}{E_{(1/2)\,\mathbf{Q}+\mathbf{k}}}\right) \times \frac{M\overline{Q}(\mathbf{Q},\mathbf{k})}{\frac{1}{4}s + \frac{1}{4}\mathbf{Q}^2 - E^2_{(1/2)\,\mathbf{Q}+\mathbf{k}} + i\varepsilon} g_{\mathbf{Q}}(\mathbf{k},\mathbf{q};\sqrt{s}). \tag{17}$$

The above Dirac-Brueckner approach differs in a nontrivial way from the conventional nonrelativistic Brueckner approach. The density dependence of the one-boson-exchange interaction by means of effective Dirac spinors and the explicit relativistic kinematics are features which have no counterpart in the traditional Brueckner approach. However, with the suppression of these relativistic dynamical effects we can extract a minimum of relativistic features needed in the nonrelativistic model. In our approach self-consistency is demanded with the following choice for the quasiparticle spectrum:

$$E_{\mathbf{p}}^2=\mathbf{p}^2+[M+U(\mathbf{p})]^2. \tag{18}$$

As in the usual Brueckner-Bethe-Goldstone approach, the quasipotential $U(\mathbf{p})$ is obtained self-consistently with the use of the continuous choice at the Fermi surface. As a first check, we consider the case of two nucleons interacting in free space, for which the Pauli blocking operator becomes the identity and the nuclear self-consistent field vanishes. Furthermore, if the interaction is described in the pair c.m. ($\mathbf{Q}=\mathbf{0}$), then the g matrix corresponds to the free scattering matrix T as described by the BbS equation [cf. Eq. (13)]. This limit is immediately verified upon substitution of $\sqrt{s}$ by $2\sqrt{q_o^2+M^2}$, with q_o the on-shell c.m. relative momentum. Thus,

$$T(\mathbf{q}',\mathbf{q};\sqrt{s})=V(\mathbf{q}',\mathbf{q}) + \int \frac{d^3k}{(2\pi)^3} V(\mathbf{q}',\mathbf{k}) \frac{M}{q_o^2-k^2+i\varepsilon} T(\mathbf{k},\mathbf{q};\sqrt{s}), \tag{19}$$

which is the nonrelativistic Lippmann-Schwinger equation with the pole at the relativistically correct momentum.

The other case of interest is infinite nuclear matter, where the relativistic structure of the quasiparticle spectrum introduced in Eq. (18) can be assessed considering the following power expansion in terms of U/M:

$$E_{\mathbf{p}}^2/M \approx 2\left(\frac{\mathbf{p}^2}{2M}+U(\mathbf{p})\right)+M[1+O((U/M)^2)]. \tag{20}$$

If we substitute $\mathbf{p}^2$ by the angle averaged quantity $\frac{1}{4}\mathbf{Q}^2+\mathbf{k}^2$ and proceed similarly with s, the similarity of the energy denominator in Eq. (17) with the one obtained using the nonrelativistic propagator is evident. An estimate of the accuracy of the above approximation at normal densities can be made considering $(U/M)\lesssim 1/10$. In such a case the above form of E^2 yields a propagator equivalent to its nonrelativistic counterpart with an accuracy better than 1%. This result supports the use of the nonrelativistic self-consistent scheme to obtain the quasipotentials.

With the above considerations, the calculation of the two-body effective interaction needed in the full-folding optical potential proceeds with the proper choice of the s invariant in Eq. (17), and consistent with the starting energy Ω_α defined in Eq. (1). Since Ω_α represents the total pair energy of interacting nucleons with total momentum $\mathbf{Q}$, the s invariant is simply given by $s=\Omega_\alpha^2-\mathbf{Q}^2$.

V. APPLICATIONS

A few remarks about the actual implementation of the computational procedures, aimed at obtaining the full-folding optical potential $U(E)$, are noteworthy. First of all, we use the Slater approximation for the nuclear mixed density $\phi^\dagger\phi$ in Eq. (1). This approximation has been discussed in the past [6] and becomes particularly suitable for the present applications, where we rely on the same point nuclear densities for the target ground state. Furthermore, we make use of the infinite nuclear matter g matrix to represent the effective interaction between the projectile and the target nucleon [6]. As a result, the g matrix evaluated at a Fermi momentum k_F is folded with the target ground state density ρ at a local momentum $\hat{k}(R)$. The Slater approximation suggests the ansatz $k_F=\hat{k}$, where the local momentum $\hat{k}$ is determined from the density by $\hat{k}^3(R)=3\pi^2\rho(R)/2$. These considerations yield for the full-folding optical model potential

$$U(\mathbf{k}',\mathbf{k};E)=4\pi\int d\mathbf{R}e^{i(\mathbf{k}'-\mathbf{k})\cdot\mathbf{R}}[\rho_p(\mathbf{R})\overline{g}_{pN}(\mathbf{k}'_r,\mathbf{k}_r) + \rho_n(\mathbf{R})\overline{g}_{nN}(\mathbf{k}'_r,\mathbf{k}_r)], \tag{21}$$

where ρ_p and ρ_n are the local proton and neutron point densities, respectively, and $\overline{g}_{NN}$ represent the off-shell Fermi-averaged amplitudes in the NN channel. For a particular channel this amplitude depends on the nuclear matter density *via* k_F (implicit in g), and the local momentum $\hat{k}$ which sets the bounds for the Fermi motion of the target nucleons. This is expressed as

$$\overline{g}_{NN}(\mathbf{k}',\mathbf{k})=\frac{3}{4\pi\hat{k}^3}\int \Theta(\hat{k}-|\mathbf{P}|)g_{\mathbf{K}+\mathbf{P}}(\mathbf{k}'_r,\mathbf{k}_r;\sqrt{s})d\mathbf{P}, \tag{22}$$

where $\mathbf{K}=(\mathbf{k}+\mathbf{k}')/2$ and the relative momentum $\mathbf{k}_r$ and $\mathbf{k}'_r$ are obtained following each of the two relativistic prescriptions discussed in Appendix A. We stress at this point that these amplitudes are calculated fully off-shell and that no assumption is made regarding the coordinate space structure of the g matrix. With these considerations the full-folding optical potential becomes a genuine nonlocal operator. Its use in the Schrödinger equation involves integrodifferential equations which are solved exactly within numerical accuracy.

The nuclear matter calculations for the g matrix were done with fully self-consistent fields at various values of k_F. We have considered the inversion potentials based upon the SP00 phase shift solution with Nijmegen-I, -II, and Reid-93 reference potentials (SP00-NIJ1, SP00-NIJ2, and SP00-RE93, respectively), Argonne reference potential (SP00-

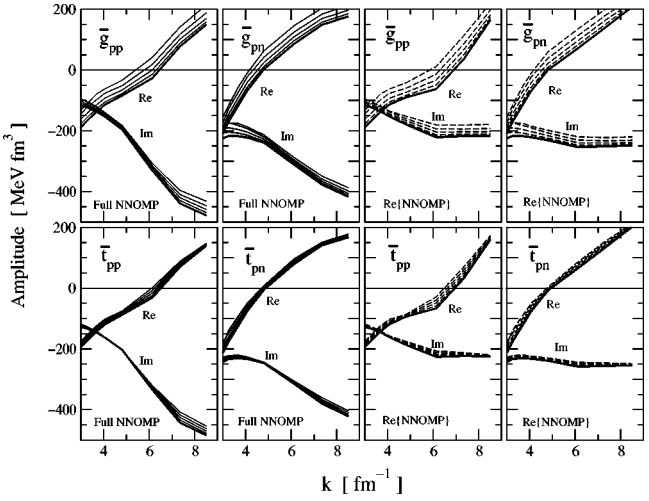

FIG. 2. The Fermi-averaged forward amplitude $\bar{g}_{NN}$ at $k_F = 1$ fm^{-1} (upper frames) and $\bar{t}_{NN}$ (lower frames) based on the SP00-AV18 NNOMP at local momenta $\hat{k} = 0.6(0.2)1.4$ fm^{-1} in the *pp* and *np* channels, and as functions of the projectile momentum. The four left-most frames represent results using the full NNOMP, whereas the four right-most frames with the dashed curves correspond to results with the imaginary part of the NNOMP suppressed. The thick solid curves denote results for $\hat{k} = 0.6$ fm^{-1}.

AV18), Paris reference potential (SP00-PARI), and Gel'fand-Levitan-Marchenko inversion reference potential (SP00-INVS).

A. Medium and Fermi motion effects

To disclose some of the features exhibited by the Fermi-averaged effective interaction in the context of the full-folding approach, we analyze the $\bar{g}$ averages in the proton-proton (*pp*) and neutron-proton (*np*) channels. Here we focus on the on-shell forward matrix element. In this case the $\bar{g}_{NN}$ amplitude depends on the NA projectile momentum $|\mathbf{k}|$, the Fermi momentum k_F, and the local momentum $\hat{k}$. In the case of the free *t*-matrix approach for the interaction we set $k_F = 0$ but allow for the variation of $\mathbf{P}$ implied by the local nuclear density to account for the Fermi motion in the nucleus ($|\mathbf{P}| \leqslant \hat{k}$). In the case of a *g*-matrix element we set $\hat{k} = k_F$. In Fig. 2 we show the real and imaginary components of $\bar{g}_{pp}$ and $\bar{g}_{np}$, based on the SP00-AV18 NNOMP, as functions of the beam momentum and for the sequence $\hat{k} = 0.6(0.2)1.4$ fm^{-1}. In each frame we draw the case $\hat{k} = 0.6$ fm^{-1} with a thick solid curve; the following values of $\hat{k}$ depart sequentially from this reference curve. The upper and lower frames correspond to *g*- and *t*-matrix results, respectively. To assess the role of the imaginary part of the NNOMP, the results based on the full model are shown in the four leftmost frames with solid curves while the results where the imaginary part is suppressed are shown in the four rightmost frames with dashed curves. The two relativistic kinematics prescriptions—Giebink and AAY—yield almost indistinguishable results for the amplitudes.

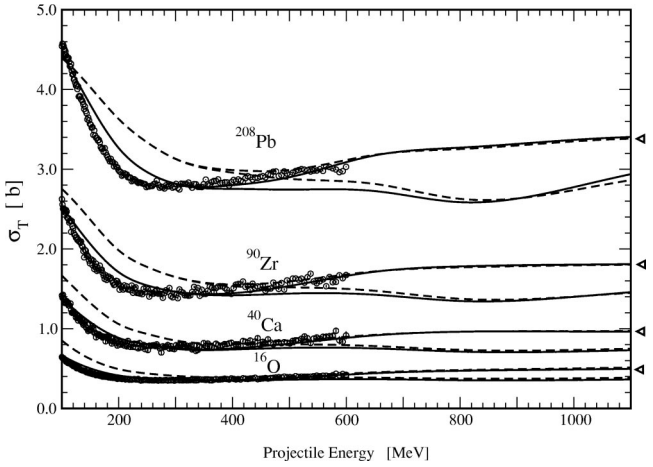

FIG. 3. Total cross section for neutron elastic scattering from ^{208}Pb, ^{90}Zr, ^{40}Ca, and ^{16}O as functions of the projectile energy. The data [29] are represented with open circles. The solid and dashed curves represent full-folding results using the *g* and *t* matrix, respectively. The curves corresponding to the full NNOMP are marked with a triangular label at their right end, whereas those results with the imaginary part of the NNOMP suppressed are unmarked.

A comparison of results in the upper and lower frames indicates more dispersion due to the Fermi motion within the *g*-matrix than in the *t*-matrix approach. This is a feature which is more pronounced in the real than the absorptive component of the amplitude. This is a clear indication of the role of the self-consistent fields in the Fermi-averaged quantities. In the context of the full NNOMP, however, the manifestation of this sensitivity becomes diminished at projectile energies above 500 MeV as the real component of all amplitudes for $|\mathbf{k}|$ above ~ 5 fm^{-1} are significantly smaller than their imaginary counterparts. Such is not the case at the lower energies, where both the real and imaginary components of the amplitude become comparable. Thus, we do expect more sensitivity under Fermi motion in the context of the *g* matrix at projectile energies below 500 MeV.

Another feature that emerges from Fig. 2 is the sensitivity of the absorptive part of $\bar{g}$ to the presence of the imaginary part of the NNOMP. Indeed, when this part is suppressed, the absorptive component of the amplitude saturates above ~ 5 fm^{-1}, in contrast with the full NNOMP where the trend of this absorption is to increase. The manifestation of this feature becomes clear when the Fermi average enters fully off-shell in the evaluation of the full-folding potential, as discussed in the following section.

B. Total cross sections

A global assessment of the full-folding model to the inclusion of relativistic kinematics and features of the underlying *NN* potential model over a wide energy range is made first by studying total cross sections for neutron-nucleus elastic scattering. In Fig. 3 we show the measured [29] and calculated total cross sections for neutron elastic scattering from ^{16}O, ^{40}Ca, ^{90}Zr, and ^{208}Pb at beam energies ranging from 100 MeV up to 1 GeV. These cross sections are obtained by

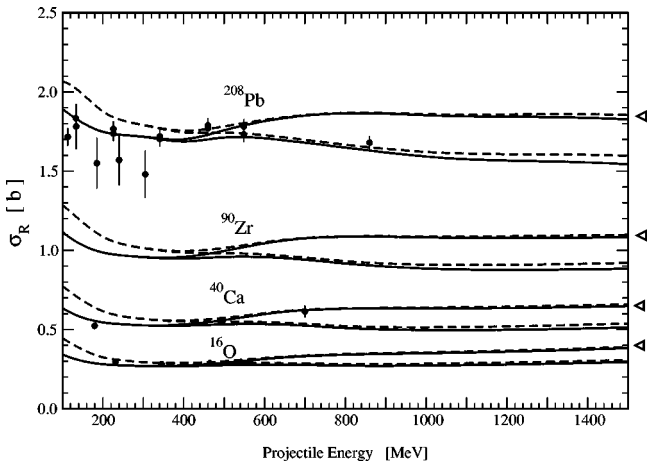

FIG. 4. Predicted reaction total cross section for proton elastic scattering from ^{208}Pb, ^{90}Zr, ^{40}Ca, and ^{16}O as functions of the beam energy. The data were taken from Ref. [30]. The solid and dashed curves represent full-folding results using the *g* and *t* matrix, respectively. The curves corresponding to results based on the full NNOMP have been marked with a triangular label at their right end, whereas those results with the imaginary part of the NNOMP suppressed are unmarked.

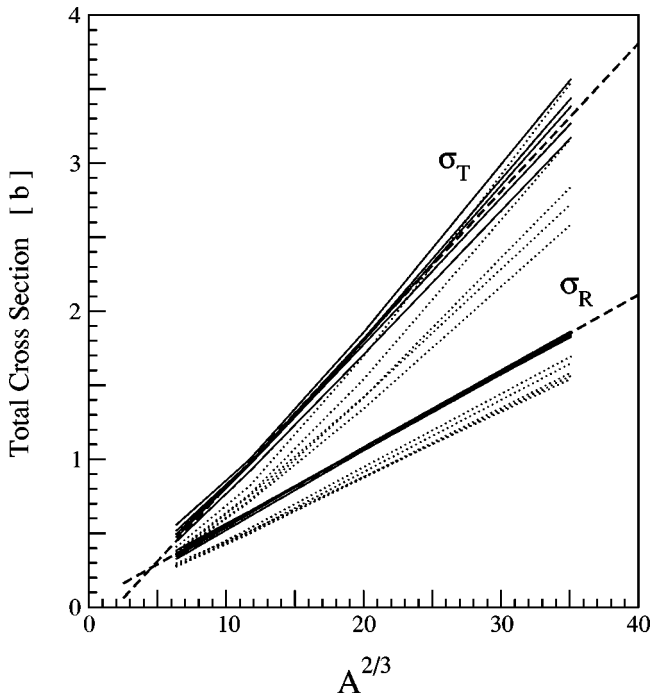

FIG. 5. The reaction cross section (σ_R) and total cross section (σ_T) for proton and neutron elastic scattering as a function of $A^{2/3}$ for projectile energies of 650, 800, 1040, 1250, and 1500 MeV. The solid and dotted curves correspond to *g*-matrix full-folding results based on the full and imaginary-suppressed NNOMP, respectively. The dashed curves correspond to straight lines in terms of $A^{2/3}$ (see text for details).

solving the scattering equations using full-folding optical potentials calculated as in Ref. [6], modified to include the kinematics discussed in this work. For completeness in this comparison we have considered the full NNOMP within the *g*- (solid curves) and *t*-matrix (dashed curves) approaches. In order to assess the role of the absorptive contribution of the NNOMP, we have also included results suppressing the imaginary part. These results are shown unmarked, whereas those using the full NNOMP have been labeled with a triangle at their right end. The data are represented with open circles. From this figure we observe a remarkable agreement between the full NNOMP *g*-matrix results and the data, particularly at energies above $\sim$200 MeV. Such is not the case for the *t*-matrix approach, or when the imaginary part of the bare *NN* potential is suppressed. In the former case the lack of nuclear medium effects becomes pronounced for projectile energies as high as 500 MeV in the case of Pb, but less for lighter nuclei. Conversely, the imaginary part of the NNOMP is crucial for the adequate description of cross section data at beam energies above 400 MeV, as observed when comparing the labeled and unlabeled curves.

Total reaction cross sections for proton-nucleus elastic scattering at high energies are of increasing interest, particularly with current trends using spallation facilities with high energy beams. Thus, we calculated the total reaction cross section for elastic proton scattering, at beam energies up to 1.5 GeV, and compare them with available data [30]. In strict analogy with the previous applications, and using the notations as in Fig. 3, in Fig. 4 we show *g*- (solid curves) and *t*-matrix (dashed curves) results that used the full or suppressed the imaginary part of the NNOMP. Here again we have marked with triangular labels those results based on the full NNOMP, and left unmarked the ones with the imaginary part suppressed. The data are represented by open circles. The results shown in Fig. 4 used the SP00-AV18 NNOMP. For this particular observable and energies of our study, we find very similar results among all the NNOMP, i.e., irrespectively of the reference potential. Again we find little differences between the *g*- and *t*-matrix approaches above $\sim$500 MeV. Thus, medium effects in the interaction are rather weak (albeit not negligible) at these higher energies. Such is not the case below 400 MeV, particularly in the case of Pb, where a clear departure of the *t*-matrix with respect to the *g*-matrix results is observed. However, these differences are smaller than the ones due to the presence of the imaginary part of the NNOMP. In fact, we can see clear differences within the *g*-matrix approach by including and suppressing the imaginary part of the NNOMP at energies above 500 MeV. Since reaction cross section data are scarce above 700 MeV (only two data points for all four targets), the curves (marked with triangles) constitute a high energy prediction of our work.

Another feature observed from Figs. 3 and 4 is the trend of all cross sections to reach a plateau above 650 MeV. We have scrutinized more closely this feature and find that both σ_T and σ_R exhibit an almost linear dependence with $A^{2/3}$, with target masses $16 \leqslant A \leqslant 208$. To illustrate this point we show in Fig. 5 the calculated σ_T and σ_R as a function of $A^{2/3}$. The solid curves represent results from *g*-matrix full-folding results, based on the SP00-AV18 full NNOMP, at various energies; the dotted curves represent the corresponding results without the imaginary part of the NNOMP. The dashed curves serve as reference and correspond to the parametric

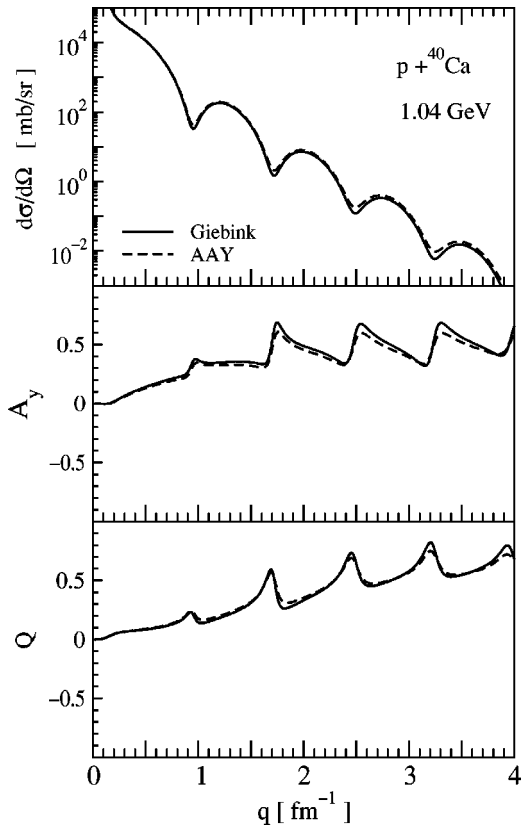

FIG. 6. Sensitivity to the kinematics: the calculated differential cross section (upper frame), analyzing power (middle frame), and spin rotation (lower frame) as functions of the momentum transfer for $p+{}^{40}$Ca elastic scattering at 1.04 GeV. The results correspond to nonrelativistic *in-medium* full-folding optical potentials using Giebink's (solid curves) and AAY (dashed curves) relativistic kinematics.

forms $\sigma_T=(-0.19+0.10A^{2/3})$ and $\sigma_R=(0.03+0.052A^{2/3})$ in barn units. Notice, only the full NNOMP results feature a moderate deviation from the parametric forms shown, which is not the case in calculations where the imaginary part of the NNOMP was suppressed (dotted curves). Thus, the absorptive part of the NNOMP inhibits the energy dependence of the total cross sections above 700 MeV.

C. Differential cross sections

Differential cross sections and spin observables for elastic scattering remain a challenge for any microscopic theory. An assessment of alternative relativistic kinematics is made with a comparison of these observables using Giebink and AAY relativistic approaches. These results are illustrated in Fig. 6, where the differential cross section $d\sigma/d\Omega$, analyzing powers A_y, and spin rotation functions Q for p+^{40}Ca elastic scattering at 1.04 GeV are shown as function of momentum transfer q. We have used g matrices together with Giebink (solid curves) and AAY (dashed curves) kinematics. This figure shows the case where the differences should be most pronounced. Indeed, all the other cases show nearly complete overlap between the two cases. Nevertheless, Fig. 6 shows that the two prescriptions yield similar results for all

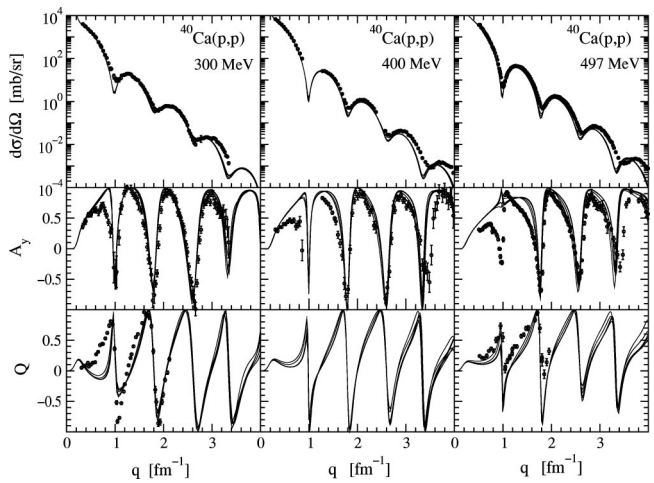

FIG. 7. Calculated differential cross section (upper frames), analyzing power (middle frames), and spin rotation (lower frames) as functions of the momentum transfer for $p+{}^{40}$Ca elastic scattering at 300 MeV, 400 MeV, and 497.5 MeV. All curves are obtained from *in-medium* full-folding optical potentials using relativistic kinematics. The data are from Ref. [31].

observables. Some differences can be seen in A_y, at momentum transfers above 1.5 fm^{-1}, where the AAY lie slightly above the Giebink kinematics results. We selected for all further calculations the Giebink kinematics.

Next, we study six NNOMP in *NA* elastic scattering at various energies with the full-folding model using the *g*-matrix approach. We have chosen scattering of protons from ^{40}Ca and ^{208}Pb for which there is a large body of high precision data over a wide energy range [31]. The applications used the full NNOMP with reference to SP00-NIJ1, -NIJ2, -PARI, -AV18, -RE93, and -INVS solutions. As in most cases the differences among these reference *NN* potentials are moderate; we have chosen all curves with a single pattern. This also helps us to illustrate the level of sensitivity of *NA* scattering upon on-shell equivalent potentials with different off-shell behavior.

Considering that the results presented here correspond to parameter free calculations, the overall description of all elastic scattering data is remarkably good. Only a close examination of the results shows the limitations of our approach. In Fig. 7 for $p+{}^{40}$Ca scattering at 300, 400, and 497.5 MeV, for instance, we observe a very good agreement between the full-folding model results for all observables and momentum transfers above ~ 1 fm^{-1}. However, some discrepancies remain in the description of low momentum transfer data. In Fig. 8 are shown $p+{}^{40}$Ca results for energies between 650 and 1040 MeV. We observe two curves slightly separated from the rest. Such curves correspond to the SP00-AV18 and SP00-PARI NNOMP, affecting mainly the differential cross section and analyzing powers at 800 and 1040 MeV. The possible cause of this feature, and the fact that this is more pronounced in the case of Ca than in Pb, is not fully understood but numerical reasons cannot be ruled out. A similar trend is observed in Fig. 9 for $p+{}^{208}$Pb scattering. These limitations have already been noticed in previous nonrelativistic full-folding calculations.

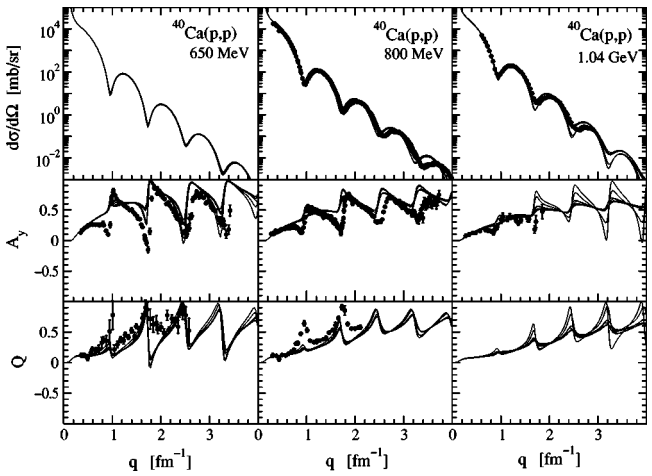

FIG. 8. The same as Fig. 7 but at 650 MeV, 800 MeV, and 1.04 GeV. The data are from Ref. [31].

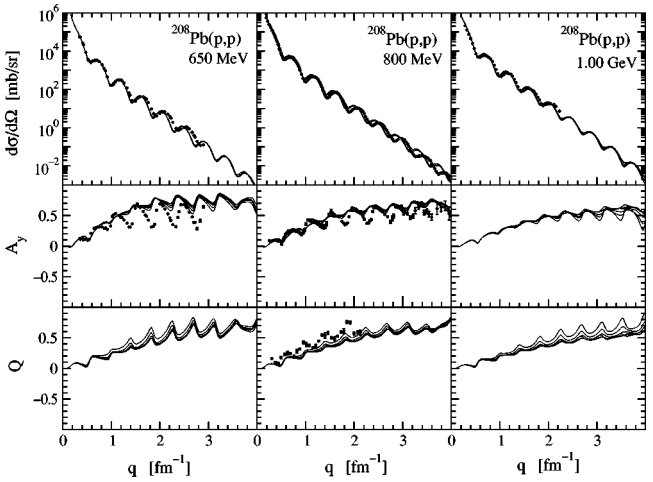

FIG. 10. The same as Fig. 9 but at 650, 800, and 1000 MeV. The data are from Ref. [31].

Thus, the identification of a unique missing element in the approaches, to account for the low q failures, remains an open issue. Some possibilities have been discussed elsewhere [5].

In Figs. 9 and 10 we show results for $p+^{208}$Pb scattering at energies between 300 MeV and 1 GeV. With the exception of the 400 and 497.5 MeV cases, the cross section is very well described by our calculations. With respect to the spin observables, there is a tendency to lose structure relative to the measured values at energies above 650 MeV.

D. Approximations

The calculation of optical potentials, within the full-folding approach used herein, are made without refuge in assumptions either about the local structure of the *NN* effective interaction or about the final structure of the *NA* coupling. In fact, these potentials are treated as nonlocal operators and are the result of a detailed account of the *NN* effective interaction off-shell. In contrast, the optical potentials in the nonrelativistic impulse approximation, discussed in Ref. [5], are assumed local and constructed with only on-shell *t*-matrix elements as effective interaction. Important differences have been observed between these two approaches when applied to intermediate energy (200–400 MeV) *NA* scattering. An illustration of these differences is made in Fig. 11 for 800 MeV $p+^{208}$Pb elastic scattering, where the differential cross section, analyzing powers, and spin rotations are shown as function of the momentum transfer. The *g*-matrix full-folding results are represented with solid curves. The *t*-matrix full-folding results are represented with long-dashed curves, whereas short-dashed and dotted curves are used to represent the results of the off-shell $t\rho$ and on-shell $t\rho$ results, respectively. Clear differences can be seen between the *g*- and *t*-matrix results, particularly for the spin observables. These are pronounced for $q \gtrsim 1.5$ fm^{-1} which illustrates the level of sensitivity to medium effects at these momentum transfers and for this particular case. Within the same *t*-matrix approach, however, the full-folding results are similar to those obtained within the $t\rho$ approximation. The extent of these sensitivities is comparable to contributions from short range correlations [5].

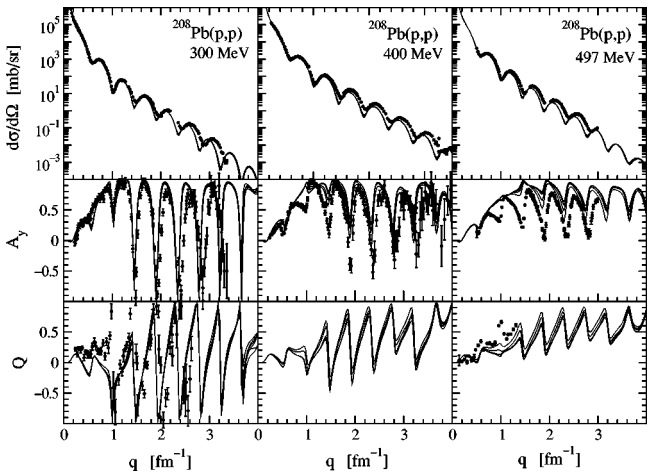

FIG. 9. Calculated differential cross section (upper frame), analyzing power (middle frame), and spin rotation (lower frame) as functions of the momentum transfer for $p+^{208}$Pb elastic scattering at 300 MeV, 400 MeV, and 497.5 MeV. All curves are obtained from *in-medium* full-folding optical potentials using relativistic kinematics. The data are from Ref. [31].

The full-folding calculations presented here are first of their kind to be tested at energies as high as $\sim$1.5 GeV. Differences are observed between these and previous results, particularly in the 800 MeV applications at forward angles [5]. Apart from the locality issue in the *NA* coupling and the treatment of the *NN* effective interaction off-shell, additional effects have been included in those local potential calculations and which may cause variations between the results. Particularly relevant seem to be the short range correlations and electromagnetic spin-orbit contributions to the *NA* coupling. A careful assessment of these effects in the context of the full-folding approach is needed. Considering that calculations in the $t\rho$ scheme are much simpler than those in the full-folding approach, the former becomes quite suitable for exploratory purposes. Quantitative comparisons, however, do

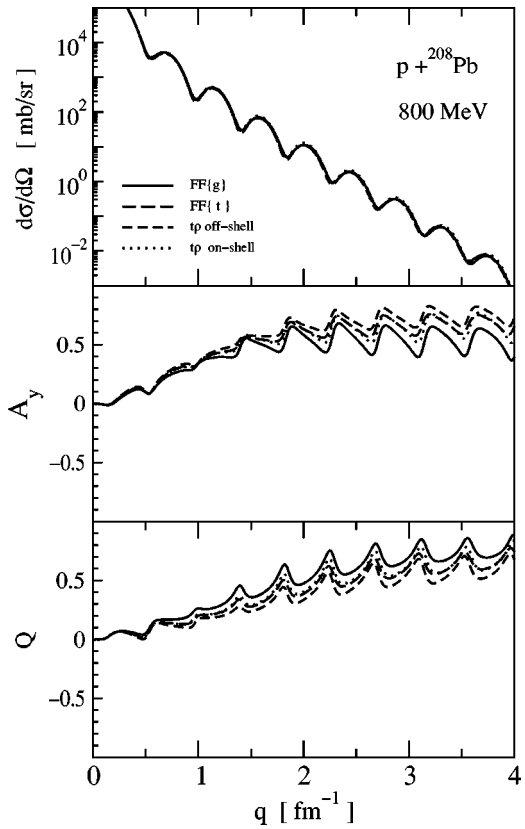

FIG. 11. A comparison of *g*-matrix full-folding (solid curves), free *t*-matrix full-folding (long-dashed curves), off-shell "$t\rho$" (short-dashed curves), and on-shell "$t\rho$" (dotted curves) results in the case of $p+^{208}$Pb elastic scattering at 800 MeV.

require the inclusion of medium effects within the full-folding approach.

VI. SUMMARY AND CONCLUSIONS

The nonrelativistic full-folding optical model approach for *NA* scattering has been extended into the relativistic regime. Kinematical issues involving the off-shell Lorentz boost of the colliding particles between the *NN* and the *NA* c.m. reference frames have been addressed. Also, explicit nuclear medium effects have been incorporated with the use of microscopic *NN* effective interaction as obtained in the framework of the nuclear matter *g* matrix using an NNOMP which fully accounts for the inelasticities and isobar resonances at nucleon energies as high as ~ 3 GeV. The nuclear matter *g* matrices were obtained considering both Pauli blocking and self-consistent nuclear fields as in the traditional Brueckner theory. Minimal relativity corrections were extracted from the Brockmann and Machleidt approach to relativistic nuclear matter. Effects arising from Wigner rotations and electromagnetic spin-orbit corrections were not included.

The study considered both *t*-matrix and *in-medium* self-consistent *g*-matrix approaches. With the inclusion of relativistic kinematics corrections, in conjunction with a realistic description of *NN* resonances and inelasticities by means of an NNOMP, we obtain a good description of both the total and the differential scattering observables for *NA* elastic scattering. The results exhibit a weak sensitivity to the choice of the relativistic approach—AAY or Giebink—to correct the kinematics. We also observe that medium effects are significant over the whole energy range of our study, although they are rather weak above 400 MeV. In contrast, the inelasticities of the *NN* interaction become important above 400 MeV as was observed particularly in the description of the total cross sections.

Although our study allows a reasonable description of the differential observables at energies as high as 1 GeV in *NA* scattering, specific details remain to be explained; notably the low q behavior of the spin observables in the 400–500 MeV range. As our primary effort has been to provide a parameter-free nonrelativistic framework for the study of *NA* elastic scattering with a minimal account of relativistic effects at these high energies, a systematic study of various other effects has not been pursued in order to keep our discussion focused. However, future work will scrutinize the systematics of the calculated observables under the use of alternative densities, mixed density representations, electromagnetic effects, and higher order correlations. Off-shell effects arising from the nonlocality range of the separable description of the NNOMP above pion threshold also require further investigation. Nevertheless, the level of agreement we have achieved, within the nonrelativistic approach, is comparable to what has been obtained within relativistic approaches.

The study presented is limited in its value as we have not used a covariant two-body and $(A+1)$-body dynamics. The approach adopted is a practical one and is largely motivated and justified by the good agreement of the numerical results with data. Thus we claim that use of minimal relativity in conjuction with *NN* optical model interactions, which fully account for the inelasticities and isobar resonances above the pion threshold, yield quantitative descriptions of *NA* scattering up to energies of 1.5 GeV.

ACKNOWLEDGMENTS

H.F.A. acknowledges partial support from FONDECYT under Grant No. 1970508. The authors thank Professor B. C. Clark and Professor L. Ray for making available much of the differential scattering data presented in this work.

APPENDIX A: RELATIVISTIC KINEMATICS

We have used two prescriptions for the relativistic kinematics involved in the transformation of the two-body colliding momenta between the pair c.m. and the projectile-nucleus c.m. These schemes have been developed by Giebink [22] and by Aaron *et al.* [20]. The latter has also been obtained by imposing time reversal invariance on the scattering amplitude [21].

Following Giebink in the context of a manifestly Lorentz invariant two-body transition amplitude, let $k=(\bar{\omega},\mathbf{k})$ and $p=(\bar{\varepsilon},\mathbf{p})$ be the projectile and struck-nucleon four-momenta in the projectile-nucleus c.m. The corresponding momenta in the exit channel are represented with k' and p'. In Giebink's

approach the total four-momentum is conserved,

$$k+p=k'+p'\equiv Q, \tag{A1}$$

which, to be valid, requires each particle to be off mass shell. The relative momenta in the two-body c.m. is readily obtained by applying a Lorentz transformation to momenta with a single boost β. This boost is obtained from the invariant

$$(\overline{\omega}+\overline{\varepsilon})^2-(\mathbf{k}+\mathbf{p})^2=S, \tag{A2}$$

and from

$$\boldsymbol{\beta}=\frac{\mathbf{k}+\mathbf{p}}{\overline{\omega}+\overline{\varepsilon}}=\frac{\mathbf{k}'+\mathbf{p}'}{\overline{\omega}'+\overline{\varepsilon}'}. \tag{A3}$$

With this velocity, a direct calculation yields for the incident ($\mathbf{k}_r$) and outgoing ($\mathbf{k}_r'$) relative momenta

$$\mathbf{k}_r=\frac{(\overline{\varepsilon}+\varepsilon_r)\mathbf{k}-(\overline{\omega}+\omega_r)\mathbf{p}}{\overline{\varepsilon}+\varepsilon_r+\overline{\omega}+\omega_r},$$

$$\mathbf{k}_r'=\frac{(\overline{\varepsilon}'+\varepsilon_r')\mathbf{k}'-(\overline{\omega}'+\omega_r')\mathbf{p}'}{\overline{\varepsilon}'+\varepsilon_r'+\overline{\omega}'+\omega_r'}. \tag{A4}$$

In these expressions the subscript r denotes the on-mass-shell relative energy

$$\omega_r=\sqrt{m_p^2+\mathbf{k}_r^2},\quad \varepsilon_r=\sqrt{m_t^2+\mathbf{k}_r^2}, \tag{A5}$$

where m_p and m_t represent the masses of the projectile and struck-nucleon, respectively. In all the above expressions the magnitude of the relative momentum $\mathbf{k}_r^2$ is needed. It can be shown that

$$\mathbf{k}_r^2=\frac{1}{4S}\xi^2(S,k^2,p^2), \tag{A6}$$

where the ξ function is defined as

$$\xi(x,y,z)=\sqrt{(x-y-z)^2-4yz}. \tag{A7}$$

Notice that the ξ function in Eq. (A6) is evaluated at the off-mass-shell invariants $k^2=\overline{\omega}^2-\mathbf{k}^2$ and $p^2=\overline{\varepsilon}^2-\mathbf{p}^2$. The actual implementation of Giebink's procedure faces the difficulty of improper Lorentz transformations that occur when S in Eq. (A2) becomes negative; this happens for very large momenta $\mathbf{k}+\mathbf{p}$. However, as the bound-state wave functions of the struck nucleons confine the momentum distribution of $\mathbf{p}$ to magnitudes below ~ 2 fm^{-1}, such improper contributions occur for very large $\mathbf{k}$ and $\mathbf{k}'$, affecting only far off-shell matrix elements in $U(\mathbf{k}',\mathbf{k})$. A way to circumvent this difficulty is to restrict S in Eq. (A2) near on-mass-shell. Thus, we approximate

$$S\approx m_p^2+m_t^2+2\overline{\omega\varepsilon}-2\mathbf{k}\cdot\mathbf{p}. \tag{A8}$$

Averaging the Fermi motion of the target nucleons ($\mathbf{p}$) allows the simplification

$$S\rightarrow S_o=m_p^2+m_t^2+2\overline{\omega\varepsilon}. \tag{A9}$$

Consistent with the above, the following forms are obtained for the relative energies:

$$\omega_r=\frac{\overline{\omega\varepsilon}+m_t^2}{\sqrt{S_o}},\quad \varepsilon_r=\frac{\overline{\omega\varepsilon}+m_p^2}{\sqrt{S_o}}. \tag{A10}$$

Clearly $\sqrt{S_o}=\omega_r+\varepsilon_r$, which is a handy result for the energy denominators in Eq. (A4). The full-folding calculations following Giebink relativistic kinematics were made using $\overline{\varepsilon}=\overline{\varepsilon'}=M$ and $\overline{\omega}=\overline{\omega'}=M+E$, with M the nucleon mass.

In the relativistic prescription developed by Aaron and collaborators [20], the relative momenta for the incoming and outgoing channels require different boost velocities. In each channel the particles are set on-mass-shell and the corresponding boost is represented by Eq. (A3). The resulting relative momentum exhibits the same structure as the one given by Eq. (A4) but with the substitution $\overline{\omega}\rightarrow\omega(\mathbf{k})$ and $\overline{\varepsilon}\rightarrow\varepsilon(\mathbf{p})$. A direct calculation yields for the magnitude

$$\mathbf{k}_r^2=\frac{1}{4s_{in}}\xi^2(s_{in},m_p^2,m_t^2), \tag{A11}$$

where

$$s_{in}=[\varepsilon(\mathbf{p})+\omega(\mathbf{k})]^2-(\mathbf{p}+\mathbf{k})^2. \tag{A12}$$

An analogous result is obtained for the outgoing channel.

APPENDIX B: ALGORITHM TO DETERMINE THE NNOMP FROM DATA

Consider that there are three distinct Hamiltonians [4]. They are the *reference* Hamiltonian H_0, a *projected* Hamiltonian H_{PP}, and a *full optical model* Hamiltonian $\mathcal{H}$. The first of these, the reference Hamiltonian $H_0:=T+V_0$, invokes a given potential V_0 for which one can find Schrödinger equation reference solutions. The physical outgoing solutions $\psi_0:=\psi_0^+(\mathbf{r},\mathbf{k},E)$ of H_0 we assume yields a unitary S matrix. We assume further that this Hamiltonian is completely specified such that evaluation of any quantity, wave function, S matrix, K matrix, etc., is facilitated. The Feshbach projection operator formalism gives the projected Hamiltonian, $PH_0P=H_{PP}$. We assume completeness, $P+Q=1$, and a finite rank representation of the Q space,

$$Q:=\sum_{i=1}^{N}|\Phi_i\rangle\Big\langle\Phi_i\Big|=\sum_{i=1}^{N}\Big|i\Big\rangle\langle i|, \tag{B1}$$

with the Q space basis functions $|\Phi_i\rangle$ interpreted as doorway states. With these doorway states we make the link between the QCD and the hadronic sectors, the latter encompassing nucleons, mesons and other free particles. Thus we assume that meson creation/annihilation occurs only in the highly

nonlinear QCD sector so that Q space wave functions are projections of such processes onto hadronic particle coordinates. The third of our Hamiltonians, the *full optical model* Hamiltonian, comprises the reference Hamiltonian H_0 and the proper optical model potential $\mathcal{V}$. That potential is complex and nonlocal, and is taken to be separable of finite rank, $\mathcal{H} := T + V_0 + \mathcal{V}(r,r';lsj,E)$.

The Schrödinger equation specified with $\mathcal{H}$ has regular physical solutions $\Psi^+ := \Psi^+(\mathbf{r},\mathbf{k},E)$ whose asymptotic boundary conditions we deem to match the *experimental* elastic channel S matrix. Specifically, for these experimental S matrices we have used the continuous solutions SP00 from the Virginia group [26]. The reference potential V_0 and separable potential form factors are still to be specified in detail with the application.

To obtain the optical potential on the basis of a given reference potential, we express first the solutions of the projected Hamiltonian in terms of the reference Hamiltonian and the *a priori* defined Q space projector. The Lippmann-Schwinger equation,

$$|\psi_P\rangle = |\psi_0\rangle - \sum_j G_0^+ |j\rangle\langle j|H_{QP}|\psi_P\rangle, \tag{B2}$$

is still very general and does not depend upon a specific representation. However, in the following we assume a partial wave expansion and the following equations are identified as radial equations with the set of quantum numbers suppressed.

As projector orthogonality $PQ = QP = 0$ implies that

$$\langle j|H_{QP}|\psi_P\rangle = \sum_i^N \{\langle\Phi|G_0^+|\Phi\rangle\}_{ji}^{-1}\langle i|\psi_0\rangle, \tag{B3}$$

the solutions of Eq. (B2) can be written in terms of $|\psi_0\rangle$ as

$$\begin{aligned}|\psi_P\rangle &= |\psi_0\rangle - \sum_{ij}^N G_0^+|i\rangle\{\langle\Phi|G_0^+|\Phi\rangle\}_{ij}^{-1}\langle j|\psi_0\rangle \\ &= |\psi_0\rangle - \sum_{ij}^N G_0^+\Lambda_{ij}|\psi_0\rangle,\end{aligned} \tag{B4}$$

wherein one can identify a separable potential

$$|i\rangle\{\langle\Phi|G_0^+|\Phi\rangle\}_{ij}^{-1}\langle j| = |i\rangle\lambda_{ij}\langle j| =: \Lambda_{ij}(r,r'). \tag{B5}$$

Note then that the definition of Q space gives a specification of the separable strengths $\lambda_{ij}(lsj,E)$ that is unique. The resultant Eq. (B4) has the form of a first order Born approximation but in fact it is an exact result.

To proceed, initially we abandon the exactitude of Eq. (B4) and require the strength matrix,

$$\lambda_{ij} = \{\langle\Phi|G_0^+|\Phi\rangle\}_{ij}^{-1}, \tag{B6}$$

to be constrained asymptotically by the experimental S matrix of the full Hamiltonian Schrödinger equation, i.e., asymptotically we induce $|\psi_P\rangle = |\Psi_{\mathcal{H}}\rangle$. This implies that complex optical model strengths λ_{ij} emerge as a result of matching to Riccati-Hankel functions and nonunitary S matrices with

$$|\Psi_{\mathcal{H}}\rangle = |\psi_P\rangle \sim \frac{1}{2i}[-h^-(rk) + h^+(rk)S(k)]. \tag{B7}$$

The strengths λ_{ij} then can be simply determined from the linear system of equations

$$\frac{1}{2i}h^+(Rk)[S(k) - S_0(k)] = \sum_{ij} G_0^+|i\rangle\lambda_{ij}\langle j|\psi_0^+\rangle. \tag{B8}$$

To reinforce a Lippmann-Schwinger equation, with the experimental S matrix as boundary condition or equivalently with strengths λ_{ij} from Eq. (B8), a transformation of the separable potential Eq. (B5) is made. This is achieved with

$$\mathcal{V}(r,r') := \Lambda\frac{1}{(1 - G_0^+\Lambda)}, \tag{B9}$$

which contains the separable potentials as defined with Eq. (B5) but whose strengths now are solutions of Eq. (B8). As the transformation Eq. (B9) contains integration of orthonormal functions, only strengths are altered. Using this optical model in the full Hamiltonian, physical solutions are obtained with reference solutions $|\psi_0\rangle$ and Green's function G_0^+ of the reference Hamiltonian H_0 by means of the Lippmann-Schwinger equation

$$|\Psi_{\mathcal{H}}\rangle = |\psi_0\rangle + G_0^+\mathcal{V}|\Psi_{\mathcal{H}}\rangle. \tag{B10}$$

[1] K. Amos, P.J. Dortmans, H.V. von Geramb, S. Karataglidis, and J. Raynal, Adv. Nucl. Phys. **25**, 275 (2000).

[2] *Proceedings of the 2nd International Conference on Accelerator-Driven Transmutation Technologies and Applications, Kalmar*, 1996, edited by H. Condé (Uppsala University, Stockholm, 1997); *Proceedings of the International Workshop on Nuclear Methods for Transmutation of Nuclear Waste: Problems, Perspectives, Cooperative Research, Dubna*, 1996, edited by M. Kh. Khankhasayev, Zh. B. Kurmanov, and H. Plendl (World Scientific, Singapore, 1997); S. G. Mashnik, A. J. Sierk, O. Bersillon, and T. Gabriel, Los Alamos Report No. LA-UR-97-2905 (http://t2.lanl.gov/publications/publications.html), contains a list of references to current major-nuclear-projects; K. A. Van Riper, S. G. Mashnik, and W. B. Wilson, Los Alamos Report No. LA-UR-98-5379.

[3] C.D. Roberts and S.M. Schmidt, Prog. Part. Nucl. Phys. **45**, 1 (2000); S. Chandrasekharan, S. Capstick, St. Dytman, R. Holt, X. Ji, J. Negele, and E. Swanson (editors), hep-ph/0012238.

[4] A. Funk, H.V. von Geramb, and K.A. Amos, Phys. Rev. C **64**, 054003 (2001).

[5] L. Ray, G.W. Hoffmann, and W.R. Coker, Phys. Rep. **212**, 223 (1992).

[6] H.F. Arellano, F.A. Brieva, and W.G. Love, Phys. Rev. Lett. **63**, 605 (1989); Phys. Rev. C **41**, 2188 (1990); **43**, 2734

(1991); **52**, 301 (1995).
[7] Ch. Elster, T. Cheon, E.F. Redish, and P.C. Tandy, Phys. Rev. C **41**, 814 (1990).
[8] R. Crespo, R.C. Johnson, and J.A. Tostevin, Phys. Rev. C **41**, 2257 (1990).
[9] M. Lacombe, B. Loiseau, J.M. Richard, R. Vinh Mau, J. Côté, P. Pirés, and R. de Tourreil, Phys. Rev. C **21**, 861 (1980).
[10] V.G.J. Stoks, R.A.M. Klomp, C.P.F. Terheggen, and J.J. de Swart, Phys. Rev. C **49**, 2950 (1994); V.G.J. Stoks, R.A.M. Klomp, M.C.M. Rentmeester, and J.J. de Swart, *ibid.* **48**, 792 (1993); V. Stoks, R. Timmermans, and J.J. de Swart, *ibid.* **47**, 512 (1993).
[11] R.B. Wiringa, V.G.J. Stoks, and R. Schiavilla, Phys. Rev. C **51**, 38 (1995).
[12] R. Machleidt, Phys. Rev. C **63**, 024001 (2001).
[13] H.F. Arellano, F.A. Brieva, M. Sander, and H.V. von Geramb, Phys. Rev. C **54**, 2570 (1996).
[14] D.P. Murdock and C.J. Horowitz, Phys. Rev. C **35**, 1442 (1987).
[15] N. Ottenstein, S.J. Wallace, and J.A. Tjon, Phys. Rev. C **38**, 2272 (1988); N. Ottenstein, E.E. van Faassen, J.A. Tjon, and S.J. Wallace, *ibid.* **43**, 2393 (1991).
[16] J.A. Tjon and S.J. Wallace, Phys. Rev. C **44**, 1156 (1991).
[17] E.D. Cooper, S. Hama, B.C. Clark, and R.L. Mercer, Phys. Rev. C **47**, 297 (1993).
[18] A.W. Thomas and R.H. Landau, Phys. Rep. **58**, 121 (1980).
[19] D.L. Weiss and D.J. Ernst, Phys. Rev. C **26**, 605 (1982).
[20] R. Aaron, R.D. Amado, and J.E. Young, Phys. Rev. **174**, 2022 (1968).
[21] D.J. Ernst and G.A. Miller, Phys. Rev. C **21**, 1472 (1980).
[22] D.R. Giebink, Phys. Rev. C **25**, 2133 (1982); **28**, 818 (1983); **32**, 502 (1985).
[23] R.A. Arndt, I.I. Strakovsky, and R.L. Workman, Phys. Rev. C **62**, 034005 (2000).
[24] H.V. von Geramb, K.A. Amos, H. Labes, and M. Sander, Phys. Rev. C **58**, 1948 (1998).
[25] M. Sander and H.V. von Geramb, Phys. Rev. C **56**, 1218 (1997).
[26] R. A. Arndt, W. J. Briscoe, R. L. Workman, and I. I. Strakovsky, Center for Nuclear Studies, Data Analysis Center [SAID program], The George Washington University, http://gwdac.phys.gwu.edu/
[27] R. Brockmann and R. Machleidt, Phys. Rev. C **42**, 1965 (1990).
[28] H. Müther, R. Machleidt, and R. Brockmann, Phys. Rev. C **42**, 1981 (1990).
[29] R.W. Finlay, W.P. Abfalterer, G. Fink, E. Montei, T. Adami, P.W. Lisowski, G.L. Morgan, and R.C. Haight, Phys. Rev. C **47**, 237 (1993).
[30] R.F. Carlson, At. Data Nucl. Data Tables **63**, 93 (1996).
[31] L. Ray and G.W. Hoffmann, Phys. Rev. C **31**, 538 (1985); D.A. Hutcheon *et al.*, Nucl. Phys. **A483**, 429 (1988); E. Bleszynski *et al.*, Phys. Rev. C **37**, 1527 (1988); G.W. Hoffmann *et al.*, Phys. Rev. Lett. **47**, 1436 (1981); A. Rahbar *et al.*, Phys. Rev. Lett. **47**, 1811 (1981); R.W. Fergerson *et al.* Phys. Rev. C **33**, 239 (1986); G.D. Alkhazov *et al.*, Nucl. Phys. **A274**, 443 (1976); G.D. Alkhazov *et al.*, Phys. Lett. **90B**, 364 (1980); O. Häusser, in *Proceedings of the Conference on Polarization Phenomena in Nuclear Physics, Paris, 1990*, edited by A. Boudard and Y. Terrien (Les Editions de Physique, Paris, 1990); B. Aas *et al.*, Nucl. Phys. **A460**, 675 (1986); N. Hintz *et al.*, University of Minnesota Summary Progress Report, 1984–1987, p. 95; University of Minnesota Progress Report, 1989; L. Ray (private communication); G.W. Hoffmann *et al.* Phys. Rev. C **21**, 1488 (1980); **24**, 541 (1981); G.D. Alkhazov *et al.*, Zap. Nauchn. Semin. LOMI **244**, 3 (1976); L. Ray *et al.*, Phys. Rev. C **23**, 828 (1981).